

Near-critical spreading of droplets

Raphael Saiseau,^{1,2} Christian Pedersen,³ Anwar Benjana,¹ Andreas Carlson,³ Ulysse Delabre,¹ Thomas Salez,^{1,*} and Jean-Pierre Delville^{1,†}

¹*Univ. Bordeaux, CNRS, LOMA, UMR 5798, F-33400, Talence, France.*

²*Laboratoire Matière et Systèmes Complexes, UMR 7057, CNRS, Université de Paris, F-75006, Paris, France.*

³*Mechanics Division, Department of Mathematics, University of Oslo, 0316, Oslo, Norway.*

We study the spreading of droplets in a near-critical phase-separated liquid mixture, using a combination of experiments, lubrication theory and finite-element numerical simulations. The classical Tanner's law describing the spreading of viscous droplets is robustly verified when the critical temperature is neared. Furthermore, the microscopic cut-off length scale emerging in this law is obtained as a single free parameter for each given temperature. In total-wetting conditions, this length is interpreted as the thickness of the thin precursor film present ahead of the apparent contact line. The collapse of the different evolutions onto a single Tanner-like master curve demonstrates the universality of viscous spreading before entering in the fluctuation-dominated regime. Finally, our results reveal a counter-intuitive and sharp thinning of the precursor film when approaching the critical temperature, which is further attributed to the vanishing spreading parameter at the critical point and the associated increasing role of critical Casimir forces in the thin precursor film.

PACS numbers:

The spreading of viscous droplets on solid substrates has been extensively studied over the last decades [1–3]. For droplet sizes smaller than the capillary length [2], the viscocapillary regime yields a self-similar asymptotic dynamics, *i.e.* the so-called Tanner's law [4], with the droplet radius R increasing in time t as $\sim t^{1/10}$. To establish this scaling, two ingredients are invoked: a global volume conservation, and a local balance at the contact line between driving capillary forces and viscous dissipation in the liquid wedge. However, such a continuous description implies a finite change of the fluid velocity over a vanishing height at the contact line, and thus leads to an unphysical divergence of viscous stress and dissipation [5]. To solve this paradox, a microscopic molecular-like cut-off length is required, and appears through a logarithmic factor in Tanner's law. In this spirit, theoretical [1, 6–12] and experimental investigations introduced various possible regularization mechanisms [13], including a gravito-capillary transition [14–17], surface roughness [16], thermal effects [18], Marangoni-driven flows [19], or a slip condition at the solid substrate [20]. In the particular case of total wetting, the existence of a thin precursor film ahead of the contact line has been proposed as a main candidate [21–23]. However, despite tremendous efforts to measure the microscopic length, or to characterize the associated logarithmic factor, the problem is still open. Conversely, solving the free-interface dynamical evolution of a droplet-like perturbation on a thin liquid film in the lubrication approximation showed that Tanner's law can be considered as a negligible-film-thickness limit of capillary levelling [24]. Such a statement was further comforted by its extension to the gravity-driven [25] and elastic-bending-driven [26] cases. As such, it is possible to unambiguously determine the microscopic precursor-film thickness from the spreading of any droplet in total-

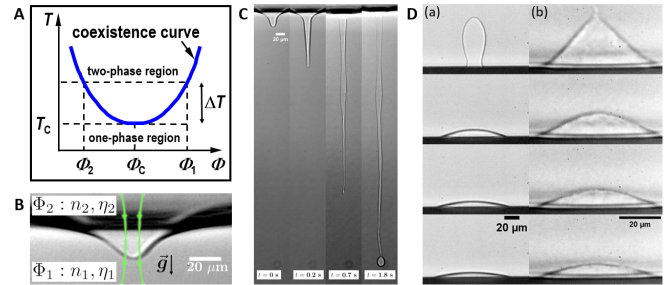


FIG. 1: **A** Schematic phase diagram of the used binary liquid mixture, where T is the temperature, Φ the micelle concentration, and T_c and Φ_c the coordinates of the critical point. **B** Radiation-pressure-induced optical bending of the interface separating the two coexisting phases at $T > T_c$, where the downward laser beam is represented by the arrows. **C** Image sequence of the optical jetting instability with drop formation at the tip. **D** Image sequences of a less-dense-phase droplet of concentration Φ_2 coalescing and spreading over a borosilicate substrate placed at the bottom of the cell, when surrounded by the denser phase of concentration Φ_1 . The temperature distances to the critical point T_c , the initial droplet volumes and the time intervals between images are: (a) $\Delta T = 8$ K, $V_{\text{ini}} = 30.3$ pL, $dt = 3$ s; (b) $\Delta T = 1$ K, $V_{\text{ini}} = 21.5$ pL, $dt = 20$ s.

wetting and lubrication conditions.

In this Letter, we investigate droplet spreading in a near-critical phase-separated binary liquid [27], with three main objectives. First, as many fluid properties vary with the proximity to a critical point according to power-law variations of the type $\sim (\Delta T/T_c)^\alpha$, with $\Delta T = T - T_c$ the temperature distance to the critical point T_c , and α some critical exponents, the spreading dynamics may be continuously and precisely tuned by varying the temperature. As a side outcome, this also

provides evidence for droplet spreading in a liquid environment, which was scarcely studied [28]. Secondly, close to a fluid-fluid critical point, an isotropic liquid belongs to the $\{d = 3, m = 1\}$ universality class of the Ising model, where d and m are respectively the space and order-parameter dimensions, so that the results are generalized to any fluid belonging to the same universality class. Thirdly, critical phenomena are often accompanied by a wetting transition at a temperature which might be either identical or distinct from the critical one [3], so that precursor films can also be investigated near the critical point.

The experimental configuration is depicted in Fig. 1. We use a water-in-oil micellar phase of microemulsion [29, 30]. At the chosen critical composition (water, 9% wt, toluene, 79% wt, SDS, 4% wt, butanol, 17% wt), it exhibits a low critical point at T_c close to 38° C, above which the mixture separates into two phases of different micelle concentrations (see Fig. 1A). The microemulsion is enclosed in a tightly-closed fused-quartz cell of 2 mm thickness (Hellma 111-QS.10X2) which is introduced in a home-made thermally-controlled brass oven with four side-by-side windows. As working in a tight cell is mandatory with critical fluids, we use a contactless optical method to create a wetting drop at the bottom wall. Note that the microemulsion is transparent (absorption coefficient smaller than $5 \cdot 10^{-4} \text{ cm}^{-1}$) at the employed wavelength. The sample is set at a temperature $T > T_c$ and a continuous frequency-doubled Nd^{3+} -YAG (wavelength in vacuum $\lambda = 532 \text{ nm}$, TEM₀₀ mode) laser beam is focused on the meniscus of the phase-separated mixture using a $\times 10$ Olympus[®] microscope objective (N.A.=0.25). The photon momentum mismatch between the two phases, proportional to the refraction-index contrast, generates a radiation pressure and the interface thus bends (see Fig. 1B) as a result from the balance between the latter with hydrostatic and Laplace pressures [31]. As the interfacial tension γ of near-critical interfaces vanishes at the critical point, with $\gamma = \gamma_0 (\Delta T/T_c)^{2\nu}$, where $\nu = 0.63$ and $\gamma_0 = 5.0 \cdot 10^{-5} \text{ N/m}$ in our case, the interfacial deformation can be made very large. When the beam propagates downwards and with sufficient power, the interface can become unstable (see Fig. 1C) due to total reflection of light within the deformation. In this case, a jet is formed, with droplets emitted at the tip [32, 33]. Note that the jetting power threshold can also be used to measure the interfacial tension [32]. The length of the jet can be tuned with the laser power to bring its tip close to the bottom of the cell, without touching it. Then, by reducing the power, the jet breaks up into many droplets due to the Rayleigh-Plateau instability. By increasing again the power, below the jetting threshold, the laser beam forces coalescence between several droplets to produce a large one which can be further pushed by radiation pressure towards a borosilicate substrate placed at the bottom

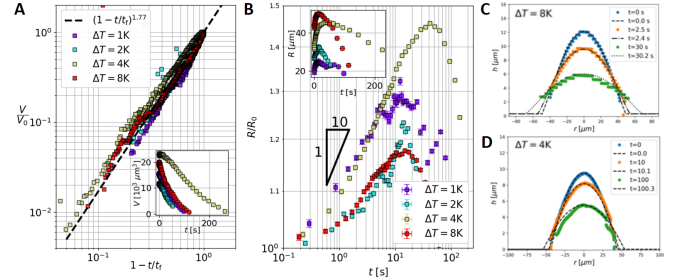


FIG. 2: **A** Rescaled droplet volume V/V_0 as a function of the rescaled time $1 - t/t_f$, with V_0 the initial volume and t_f the time of final evaporation, for four different distances to the critical temperature. The dashed line indicates the empirical power law $(1 - t/t_f)^{1.77}$. Inset: corresponding raw data. **B** Contact radius, divided by its initial value R_0 , as a function of time for the same temperatures. The $1/10$ power-law exponent of Tanner’s law is indicated with a slope triangle. Inset: corresponding raw data. **C,D** Droplet profiles at different times obtained from experiments (symbols) and compared to the numerical solutions of Eq. (1) (dashed/dotted lines) for $\Delta T = 8 \text{ K}$ (**C**) and $\Delta T = 4 \text{ K}$ (**D**).

of the cell (see Fig. 1D). We turn off the laser just before contact, and follow the droplet spreading using $\times 20$ or $\times 50$ Olympus[®] microscope objectives, with resolutions of 1.0 and 0.8 μm respectively, and a Phantom[®] VEO340L camera for the frame grabbing. Note the existence of a prewetting film on the substrate, at least up to $\Delta T = 15 \text{ K}$ [34].

Figure 1D displays two image sequences corresponding to the coalescence and spreading of droplets at $\Delta T = 8 \text{ K}$ and 1 K. The spreading time scale comparatively increases by approximately one order of magnitude for $\Delta T = 1 \text{ K}$, as a result of the vanishing interfacial tension near T_c . We also notice that the droplet volumes reduce over time, indicating the presence of evaporation, as expected for finite-size objects in an environment at thermodynamic equilibrium. At the early stages, both profiles display large curvature gradients. Since our focus here is on the long-term asymptotic spreading behavior, we define the temporal origin $t = 0$ from a first experimental image where the curvature is homogeneous, except near the contact-line region, and a spherical-cap fit is valid.

Each image sequence is then treated using a custom-made automatized contour detection based on a Canny-threshold algorithm, where the droplet profiles correspond to the external maxima of the intensity gradients. Spherical-cap fits allow to extract the droplet volume $V(t)$, radius $R(t)$, and apparent contact angle $\theta(t)$, which are then averaged using a custom-made exponentially-increasing time window to get a logarithmically-distributed data set. In the inset of Fig. 2A, we plot the experimental droplet volume as a function of time, for four different values of ΔT . In all cases, the volume decreases until the droplet is fully evap-

orated. By defining the time of final evaporation as t_f , we then plot in the main panel the same data in dimensionless form, with V/V_0 as a function of $1 - t/t_f$. We observe a data collapse onto a unique power-law behavior, with fitted exponent 1.77 which is close to the $11/7$ value theoretically predicted for evaporating droplets [11]. In Fig. 2B, we further plot the contact radius R , normalized by its initial value R_0 , as a function of time, for all ΔT . A Tanner-like power law systematically emerges at intermediate times, until evaporation eventually dominates the evolution. This observation indicates that evaporation is an quasi-static process compared to spreading, within the explored temperature range.

To model the observed spreading dynamics, we consider a large initial droplet-like interfacial perturbation profile $d(r, t = 0)$, with r the radial coordinate, atop a flat thin film of thickness ϵ , and describe its evolution through the profile $d(r, t)$ at all times, in the small-slope limit within the lubrication approximation [2]. Therein, a horizontal Newtonian viscous flow of viscosity η is driven by the gradient of Laplace pressure. Since most of the dissipation occurs in the wedge-like region near the apparent contact line [5], we further neglect the influence of viscous shear stresses in the surrounding phase. The evolution is then described by the axisymmetric capillary-driven thin-film equation [24]:

$$\partial_t h + \frac{\gamma}{3\eta r} \partial_r \left[r h^3 \partial_r \left(\frac{1}{r} \partial_r h + \partial_r^2 h \right) \right] = \mathcal{H}(1 - R) f, \quad (1)$$

where $h(r, t) = \epsilon + d(r, t)$ is the free-interface height from the solid substrate, $\mathcal{H}(1 - R)$ is the Heaviside step function with $R(t)$ the advancing radius of the droplet, and $f(t)$ is an added coefficient accounting for evaporation. The latter is chosen in order to precisely mimic the experimentally-measured evaporation (see Fig. 2A). Equation (1) is numerically integrated using a finite-element solver [35]. The experimental radial profiles depicted in Fig. 1D are chosen as initial profiles, after angular averaging and smoothening using fourth-order polynomials in order to avoid unphysical fluctuations related to the camera resolution and the contour-detection algorithm. As shown in Figs. 2C and D, the comparisons between the experimental and numerical evolutions reveal an excellent agreement. As the capillary velocity $v_{\text{cap}} = \gamma/\eta$ is independently evaluated (see [29] for the viscosity calibration), and typically varies between 22 and 1013 $\mu\text{m/s}$ for near-critical droplets within the $\Delta T = 1 - 8$ K range, the precursor-film thickness ϵ remains the only fit parameter in this comparison, and its behaviour with temperature will be discussed after.

Tanner's law [1, 4] can be obtained from the combination of: i) a local power balance between capillary driving and viscous damping near the contact line; and ii) the global volume conservation. The former power balance reduces to the Cox-Voinov's law for total-wetting

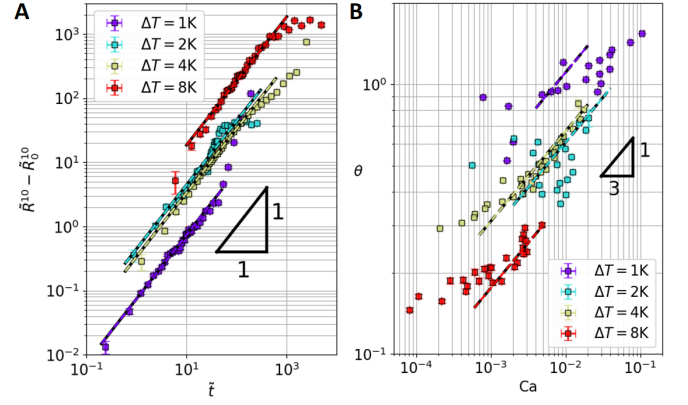


FIG. 3: **A** Rescaled contact radius $\tilde{R}^{10} - \tilde{R}_0^{10}$ as a function of rescaled time \tilde{t} , for various temperatures ΔT as indicated. The dashed lines indicate fits to Eq. (4), with ℓ as a free parameter for each temperature. **B** Contact angle θ as a function of capillary number Ca , for various temperatures ΔT as indicated. The dashed lines indicate the predictions of Eq. (2), using the ℓ values obtained from the fits in **A**.

conditions:

$$\theta^3 = 9\ell Ca, \quad (2)$$

where $Ca = \dot{R}/v_{\text{cap}}$ is the capillary number, and $\ell = \ln(L/\epsilon)$ is the logarithmic factor discussed in the introduction relating the two cut-off lengths of the problem, namely a typical macroscopic size L of the system and a microscopic length which is identified to the precursor-film thickness ϵ in total-wetting conditions.

To disentangle evaporation, through the $V(t)$ behaviour obtained in Fig. 2A, from the spreading dynamics, we introduce the following dimensionless variables:

$$\tilde{R} = R \left[\frac{\pi}{4V(t)} \right]^{1/3}, \quad \tilde{t} = v_{\text{cap}} t \left[\frac{\pi}{4V(t)} \right]^{1/3}. \quad (3)$$

Tanner's law [1, 4] is then written in dimensionless form as:

$$\tilde{R}^{10} - \tilde{R}_0^{10} = \frac{10}{9\ell} \tilde{t}, \quad (4)$$

with $\tilde{R}_0 = \tilde{R}(t = 0)$. In Fig. 3A, we plot the rescaled contact radius as a function of rescaled time, for various temperatures. We systematically observe Tanner behaviours. Interestingly, from the fits to Eq. (4), we obtain increasing values of ℓ as the critical point is neared. This trend is further confirmed in Fig. 3B, where we see Cox-Voinov behaviours (see Eq. (2)) at large-enough Ca , with an identical evolution of ℓ with ΔT . The departure from Cox-Voinov's law at low Ca is due to the evaporation-induced non-monotonic behavior of $R(t)$ (see Fig. 2B), resulting in Ca crossing zero for finite values of θ .

Using the ℓ values obtained from the Tanner fits above, we can then represent all the data onto a single master

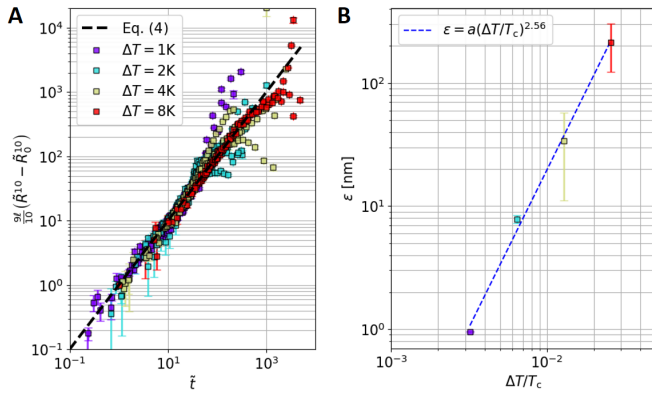


FIG. 4: **A** Dimensionless Tanner master curve including the experiments at all temperatures. The dashed line corresponds to Eq. (4). The values of the logarithmic factor ℓ were first obtained by fitting the individual experimental data in Fig. 3A to Eq. (4). **B** Extracted precursor-film thickness ϵ as a function of the temperature distance ΔT to the critical point, as obtained by fitting individual experimental profiles to numerical solutions of Eq. (1) (see Figs. 2C and D). The dashed line indicates the empirical power law $\epsilon = a(\Delta T/T_c)^{2.56}$ with $a = 2.55$ mm.

curve, as shown in Fig. 4A. The observed collapse, over more than two orders of magnitude in time and broad ranges of material parameters, shows the surprising robustness of Tanner’s law in the vicinity of the critical point, despite the increasing roles of evaporation, gravity and fluctuations.

Finally, Fig. 4B shows the extracted precursor-film thickness ϵ as a function of $\Delta T/T_c$. Strikingly, over the considered temperature range, we observe a sharp decrease of ϵ from a fraction of micrometers down to a nanometer, as the critical point is approached from above. Over a decade in the considered temperature range, this behaviour is consistent with the empirical power law $\epsilon = a(\Delta T/T_c)^{2.56}$, where $a = 2.55$ mm. Interestingly, the wetting transition in our system being located far above the largest temperature studied here [34], we would have instead expected an increase of ϵ , since the precursor film is here made of the most-wetting phase [3, 36]. This apparent contradiction may in fact reveal the existence of an original scenario in the immediate vicinity of the critical point, with at least two possible and non-exclusive ingredients. First, and provided that one can extrapolate the definition of interfaces towards the critical point, the spreading parameter [1] is expected to strictly vanish at that point, since the two fluid phases become indistinguishable media. Secondly, while the macroscopic droplet spreading appeared above to be well described by the classical Tanner’s law, critical Casimir forces may become important in the near-critical and ultra-thin precursor film. Indeed, Casimir thinning has been experimentally and theoretically demonstrated [37–39] when the critical point is neared from the two-phase

region, as soon as $\epsilon \approx \xi$, where $\xi = \xi_0(\Delta T/T_c)^{-\nu}$ is the correlation length of density fluctuations. For our micellar phase, $\xi_0 = 2.1$ nm, so that ϵ/ξ starts from 10 ($\Delta T = 8$ K), reaches 1 ($\Delta T = 4$ K), before decreasing to 0.16 ($\Delta T = 2$ K) and even 0.01 ($\Delta T = 1$ K). As such, beyond revealing the universality of viscous spreading near a critical point, our results pave the way towards further investigations closer to that point, with the aims of disentangling the different mechanisms highlighted above, as well as addressing the increasing contributions of gravity, evaporation, and eventually thermal fluctuations [40–42].

ACKNOWLEDGMENTS

The authors thank Julie Jagielka, Eloi Descamps and Thomas Guérin for preliminary work and interesting discussions, as well as the LOMA mechanical and electronic workshops for their technical contributions. The authors acknowledge financial support from the European Union through the European Research Council under EMet-Brown (ERC-CoG-101039103) grant. Views and opinions expressed are however those of the authors only and do not necessarily reflect those of the European Union or the European Research Council. Neither the European Union nor the granting authority can be held responsible for them. The authors also acknowledge financial support from the Agence Nationale de la Recherche under FISICS (ANR-15-CE30-0015-01), EMetBrown (ANR-21-ERCC-0010-01), Softer (ANR-21-CE06-0029) and Fricolas (ANR-21-CE06-0039) grants. Finally, they thank the Soft Matter Collaborative Research Unit, Frontier Research Center for Advanced Material and Life Science, Faculty of Advanced Life Science at Hokkaido University, Sapporo, Japan.

* Electronic address: thomas.salez@cnrs.fr

† Electronic address: jean-pierre.delville@u-bordeaux.fr

- [1] P.-G. De Gennes, *Reviews of modern physics* **57**, 827 (1985).
- [2] A. Oron, S. H. Davis, and S. G. Bankoff, *Reviews of modern physics* **69**, 931 (1997).
- [3] D. Bonn, J. Eggers, J. Indekeu, J. Meunier, and E. Rolley, *Reviews of modern physics* **81**, 739 (2009).
- [4] L. Tanner, *Journal of Physics D: Applied Physics* **12**, 1473 (1979).
- [5] C. Huh and L. E. Scriven, *Journal of colloid and interface science* **35**, 85 (1971).
- [6] O. Voinov, *Fluid dynamics* **11**, 714 (1976).
- [7] H. P. Greenspan, *Journal of Fluid Mechanics* **84**, 125 (1978).
- [8] L. Hocking, *The Quarterly Journal of Mechanics and Applied Mathematics* **36**, 55 (1983).
- [9] M. Brenner and A. Bertozzi, *Physical review letters* **71**, 593 (1993).

- [10] D. Quéré, Annual review of materials research **38**, 71 (2008).
- [11] A.-M. Cazabat and G. Guena, Soft Matter **6**, 2591 (2010).
- [12] E. Jambon-Puillet, O. Carrier, N. Shahidzadeh, D. Brutin, J. Eggers, and D. Bonn, Journal of Fluid Mechanics **844**, 817 (2018).
- [13] P. J. Haley and M. J. Miksis, Journal of Fluid Mechanics **223**, 57 (1991).
- [14] J. Lopez, C. A. Miller, and E. Ruckenstein, Journal of Colloid and Interface Science **56**, 460 (1976).
- [15] H. E. Huppert, Journal of Fluid Mechanics **121**, 43 (1982).
- [16] A. Cazabat and M. C. Stuart, The Journal of Physical Chemistry **90**, 5845 (1986).
- [17] P. Levinson, A. Cazabat, M. C. Stuart, F. Heslot, and S. Nicolet, Revue de physique appliquée **23**, 1009 (1988).
- [18] P. Ehrhard, Journal of Fluid Mechanics **257**, 463 (1993).
- [19] P. Kavehpour, B. Ovrzyn, and G. H. McKinley, Colloids and Surfaces A: Physicochemical and Engineering Aspects **206**, 409 (2002).
- [20] J. D. McGraw, T. S. Chan, S. Maurer, T. Salez, M. Benzaquen, E. Raphaël, M. Brinkmann, and K. Jacobs, Proceedings of the National Academy of Sciences **113**, 1168 (2016).
- [21] D. Ausserré, A. Picard, and L. Léger, Physical review letters **57**, 2671 (1986).
- [22] L. Leger, M. Erman, A. M. Guinet-Picard, D. Ausserre, and C. Strazielle, Phys. Rev. Lett. **60**, 2390 (1988).
- [23] J.-D. Chen and N. Wada, Physical review letters **62**, 3050 (1989).
- [24] S. L. Cormier, J. D. McGraw, T. Salez, E. Raphaël, and K. Dalnoki-Veress, Physical review letters **109**, 154501 (2012).
- [25] N. Bergemann, A. Juel, and M. Heil, Journal of Fluid Mechanics **843**, 1 (2018).
- [26] C. Pedersen, J. F. Niven, T. Salez, K. Dalnoki-Veress, and A. Carlson, Phys. Rev. Fluids **4**, 124003 (2019), URL <https://link.aps.org/doi/10.1103/PhysRevFluids.4.124003>.
- [27] A. Kumar, H. R. Krishnamurthy, and E. S. R. Gopal, Physics Reports **98**, 57 (1983).
- [28] H. Chaar, M. R. Moldover, and J. W. Schmidt, The Journal of chemical physics **85**, 418 (1986).
- [29] J. Petit, D. Rivière, H. Kellay, and J.-P. Delville, Proceedings of the National Academy of Sciences **109**, 18327 (2012).
- [30] R. Saiseau, Ph.D. thesis, Université de Bordeaux (2020).
- [31] H. Chraïbi, D. Lasseux, R. Wunenburger, E. Arquis, and J.-P. Delville, The European Physical Journal E **32**, 43 (2010).
- [32] A. Giroto, J. Petit, R. Saiseau, T. Guérin, H. Chraïbi, U. Delabre, and J.-P. Delville, Physical Review Letters **122**, 174501 (2019).
- [33] R. Wunenburger, B. Issenmann, E. Brasselet, C. Loussert, V. Hourtane, and J.-P. Delville, Journal of Fluid Mechanics **666**, 273 (2011).
- [34] A. Casner and J.-P. Delville, EPL (Europhysics Letters) **65**, 337 (2004).
- [35] C. Pedersen, S. Ren, Y. Wang, A. Carlson, and T. Salez, Physical Review Fluids **6**, 114006 (2021).
- [36] Y. Hennequin, D. Aarts, J. Indekeu, H. Lekkerkerker, and D. Bonn, Physical review letters **100**, 178305 (2008).
- [37] A. Mukhopadhyay and B. M. Law, Physical Review E **62**, 5201 (2000).
- [38] S. Rafai, D. Bonn, and J. Meunier, Physica A **386**, 31 (2007).
- [39] C. Hertlein, L. Helden, A. Gambassi, S. Dietrich, and C. Bechinger, Nature **451**, 172 (2008).
- [40] B. Davidovitch, E. Moro, and H. A. Stone, Physical review letters **95**, 244505 (2005).
- [41] A. M. Willis and J. Freund, Journal of Physics: Condensed Matter **21**, 464128 (2009).
- [42] S. Nesic, R. Cuerno, E. Moro, and L. Kondic, The European Physical Journal Special Topics **224**, 379 (2015).